Post-wildfire surface deformation at Batagay, Eastern Siberia, detected by L-band and C-band InSAR

Kazuki Yanagiya[1] and Masato Furuya[1]

[1]Hokkaido University

November 30, 2022

Abstract

Thawing of ice-rich permafrost can form a characteristic landform called a thermokarst. The impact of wildfire on thermokarst development remains uncertain. Here we report on the post-wildfire ground deformation associated with the 2014 wildfire near Batagay, Sakha Republic, Eastern Siberia. We used Interferometric Synthetic Aperture Radar (InSAR) to generate both long-term and short-term deformation maps, and examine the temporal evolution of the post-wildfire ground deformation over the permafrost area. Based on two independent satellite-based microwave sensors, we could validate the measurement uncertainties without relying on in-situ data. The inferred time-series based on L-band ALOS2 InSAR data indicated that cumulative subsidence has been greater than 30 cm since October 2015 at the area of greatest deformation, and that the rate of subsidence is slowed in 2018. Meanwhile, C-band Sentinel-1 InSAR data showed that the temporal evolution was not simply linear but rather include episodic changes. Moreover, we could unambiguously detect frost heave signals that were clearly enhanced inside the burned area during the early freezing season but were absent in the mid-winter. We could reasonably interpret the InSAR-based frost heave signals within a framework of premelting dynamics.

Post-wildfire surface deformation at Batagay, Eastern Siberia, detected by L-band and C-band InSAR

Kazuki Yanagiya[1] and Masato Furuya[2]

[1]Department of Natural History Sciences, Graduate School of Science, Hokkaido University.

[2]Department of Earth and Planetary Dynamics, Faculty of Science, Hokkaido University.

Corresponding author: Kazuki Yanagiya (k.yanagiya@frontier.hokudai.ac.jp) and Masato Furuya (furuya@sci.hokudai.ac.jp)

Key Points:

- Post-wildfire surface deformation on the northwest of Batagay, Eastern Siberia, was detected by two independent Interferometric Synthetic Aperture Radar systems.
- L-band long-term and C-band short-term interferograms indicate the spatial and temporal complexity of the deformation in terms of both subsidence and uplift.
- Consistency between L-band HH- and C-band VV-interferograms from distinct orbits validates a dominance of vertical displacement by more than 30 cm at maximum without in-situ measurement.
- Unambiguous detection of a frost heave signal; herein is its interpretation based on premelting dynamics.

Abstract

Thawing of ice-rich permafrost can form a characteristic landform called a thermokarst. The impact of wildfire on thermokarst development remains uncertain. Here we report on the post-wildfire ground deformation associated with the 2014 wildfire near Batagay, Sakha Republic, Eastern Siberia. We used Interferometric Synthetic Aperture Radar (InSAR) to generate both long-term and short-term deformation maps, and examine the temporal evolution of the post-wildfire ground deformation over the permafrost area. Based on two independent satellite-based microwave sensors, we could validate the measurement uncertainties without relying on in-situ data. The inferred time-series based on L-band ALOS2 InSAR data indicated that cumulative subsidence has been greater than 30 cm since October 2015 at the area of greatest deformation, and that the rate of subsidence is slowed in 2018. Meanwhile, C-band Sentinel-1 InSAR data showed that the temporal evolution was not simply linear but rather include episodic changes. Moreover, we could unambiguously detect frost heave signals that were clearly enhanced inside the burned area during the early freezing season but were absent in the mid-winter. We could reasonably interpret the InSAR-based frost heave signals within a framework of premelting dynamics.

Plain Language Summary

Wildfires in arctic regions not only show an immediate impact on nearby residents but also long-lasting effects on both regional ecosystems and landforms of the burned area via permafrost degradation and subsequent surface deformation. However, the observations of post-wildfire ground deformations have been limited. Using satellite-based imaging technique called Interferometric Synthetic Aperture Radar (InSAR), we detected the detailed spatial-temporal evolution of post-wildfire surface deformation in Eastern Siberia, which helps in understanding permafrost degradation processes over remote areas. Post-wildfire areas are likely to be focal points of permafrost degradation in the Arctic that can last many years.

1 Introduction

Wildfires in boreal and arctic regions are known to have increased over recent decades in terms of both frequency and areal coverage (e.g., Kasischke & Turetsky, 2006; Hu et al., 2010), and have had significant impacts on permafrost degradation (e.g., Jafarov et al., 2013; Zhang et al., 2015; Gibson et al., 2018). Although fires do not directly heat up the subsurface space, severe burning decreases surface albedo, and removes vegetation and surface organic soil layer that had previously acted as insulators preventing permafrost from thawing. Subsequent increases in both soil temperature and thickness of the active layer, a near-surface layer that undergoes a seasonal freeze-thaw cycle, have been documented even years after the fire (e.g., Yoshikawa et al., 2002). Moreover, in ice-rich permafrost regions, the thawing of permafrost or the melting of massive ice can lead to formation of characteristic landforms such as depressions, swamps, and slumps. While there are a variety of classifications in terms of morphological and hydrological characteristics (Jorgenson, 2013), we collectively term those thaw-related landforms as “thermokarst”. However, the role of wildfires in developing thermokarst remains quantitatively uncertain. Only a few studies have reported on subsidence signal as a development of thermokarst associated with Alaskan wildfires (Liu et al., 2014; Jones et al., 2015; Iwahana et al., 2016; Molan et al., 2018), and no such reports have been found on Siberian fires, to our knowledge. Moreover, in comparison to the controlled warming experiments in Alaska (Hinkel and Hurd Jr, 2006; Wagner et al., 2018), wildfires in arctic regions may also be viewed as uncontrolled warming experiments, which will aid in understanding the permafrost degradation processes.

Ice-rich permafrost deposits, known as the Yedoma Ice Complex (Yedoma), are widely distributed in the lowland of Alaska and Eastern Siberia (Schirrmeister et al., 2013). The greatest subsidence after the 2007 Anaktuvuk River tundra fire was, indeed, identified in the area of the Yedoma upland by LiDAR (Jones et al., 2015). Yedoma is a unique permafrost deposit in terms of its extraordinarily high volume of ice (50-90 %) and organic-rich sediments. While the organic carbon trapped in permafrost regions is estimated to be twice that in the current atmosphere, permafrost thawing and related thermokarst processes may release the carbon as greenhouse gasses (CO_2 and CH_4) via microbial breakdown, which may further promote global warming (Mack et al., 2011; Schuur et al., 2015). Antonova et al (2018), Strozzi et al (2018) and Chen et al (2018) reported subsidence signals near Yedoma-rich Lena River Delta, which are, however, not associated with wildfires.

We should note that Yedoma deposits are also found further inland. Near the village of Batagay, Sakha Republic, Eastern Siberia (Figure 1), there exists the Batagaika megaslump, known as the world’s largest retrogressive thaw slump, exposing roughly 50-90 m thick permafrost deposits (e.g., Kunitsky et al., 2013; Murton et al., 2017). Thaw slumps are characterized by a steep headwall surrounding a slump floor and develop as a result of rapid permafrost thawing. The Batagaika megaslump was initiated at the end of 1970s but still appears to be growing (Günther et al., 2016). Hence, the question arises a question as to whether nearby areas will also undergo similar thermokarst processes from any disturbances.

The objective of this study was to demonstrate the spatial and temporal changes of not only inter-annual subsidence, but also seasonal subsidence-uplift cycles associated with the wildfire of July 2014 near the village of Batagay. We used satellite Interferometric Synthetic Aperture Radar (InSAR), as in previous reports, to ascertain thermokarst development. In contrast to previous studies, we employed two independent SAR imageries with distinct carrier frequencies and polarizations, L-band (1.2 GHz) HH- and C-band (5.4 GHz) VV-polarized microwave. Moreover, the imaging geometries were different and had different sensitivities to the 3D displacement vector. Thus, we could not only take advantage of each sensor's performance in mapping deformation signals, but also could evaluate measurement accuracy without in-situ data.

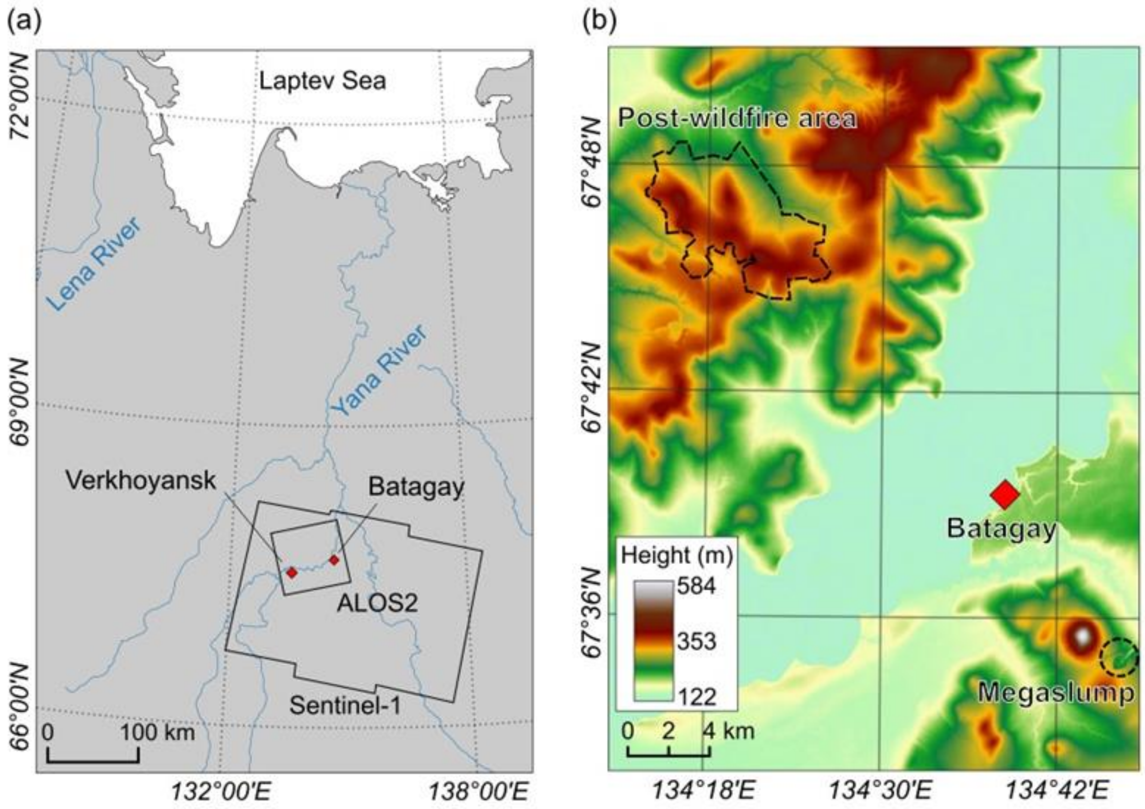

Figure 1. (a) Study area in Eastern Siberia. Black boxes indicate the imaging areas taken by each satellite. Batagay and Verkhoyansk (red diamonds) located in the imaging area. (b) Elevation map around Batagay based on a TanDEM-X DEM (12m mesh). The Batagaika megaslump is 15 km southeast of Batagay. Deformation signals due to the wildfire in July 2014 were detected in the black dashed area.

Surface deformation signals over permafrost areas have been interpreted as being caused by two major processes: (1) irreversible subsidence due to thawing of ice-rich permafrost or excess ice and (2) seasonally cyclic subsidence and uplift (Liu et al., 2014, 2015; Molan et al., 2018). In these previous reports, however, quality interferograms were limited in terms of both the temporal coverage and resolution because of the infrequent image acquisitions and the long spatial baseline problem in the Japanese Advanced Land Observation Satellite (ALOS) operated from 2006 to 2011 by the Japan Aerospace Exploration Agency (JAXA). For instance, Liu et al (2015) assumed a simple linear subsidence trend in their inversion, probably because of the limitation in temporal coverage. Moreover, the 1.5-year temporal coverage in Molan et al (2018) would be not long enough to resolve the detailed temporal evolution. Hence, the total thawed ice volume estimates were uncertain. Furthermore, no clear uplift signals have been shown in previous studies as interferometric coherence was lost during the freezing season in analyzed areas. In contrast, this study provides the first unambiguous detection of upheaval signals in the early freezing season.

Given the clear frost heave signals, we were led to interpret more physically the observed data. This was because it has been widely accepted that frost heave is unrelated to volume expansion of pre-existing pore water into ice, but caused, instead, by ice lens formation due to the migration of water (Taber, 1929, 1930). However, a physical understanding of frost heave mechanisms has been established only during recent decades (e.g., Dash, 1989; Worster and Wettlaufer, 1999; Rempel et al., 2004, Wettlaufer and Worster, 2006; Dash et al., 2006; Rempel, 2007). Here, we apply the simple but physics-based 1D theory of Rempel et al (2004) to the observed frost heave signal to physically interpret and explain the observed signals using reasonable parameters.

2 Study Site and Data Analysis

2.1 Study Site: the July 2014 wildfire on the NW Batagay

The wildfire occurred in July 2014 over a 36 km^2 area to the northwest of Batagay, Sakha Republic, Eastern Siberia (Figure 1). We could identify the occurrence of wildfire in the Landsat and MODIS optical images taken between July 17 and August 2, 2014. While wildfires in northeastern Siberia are often attributed to human activity (Cherosov et al., 2010), the onset of the July 2014 wildfire is uncertain. It is true, however, that the number of days with high flammability has noticeably increased over large portions of Russia, including the Far East (Roshydromet, 2008). We should also note that even larger nearby areas have experienced wildfires in 2019 (Siberian Times, 2019).

We have no in-situ observation data from the unburned period. However, the site is approximately 25 km to the northwest of the Batagaika megaslump (Figure 1); thus, we refer to Murton *et al* (2017)'s summary as a proxy for basic information on the burned area and permafrost. The open forest is dominated by larch with shrubs and lichen moss ground cover. The permafrost in the Yana River valley is continuous with the mean annual ground temperature at the top of permafrost, ranging from -5.5 °C to -8.0 °C, with the active layer thicknesses (ALT) beneath the forest/moss cover and open sites being 20-40 cm and 40-120 cm, respectively.

The regional climate is highly continental with a mean annual temperature of -15.4 °C and mean annual precipitation of 170 – 220 mm (Murton et al., 2017). As proxy meteorological data, we used the data at Verkhoyansk, 55 km west of Batagay. The temperature and precipitation in July/December 2017 were 12/-44 °C and 30/6 mm, respectively.

2.2 InSAR Data Sets and Analysis

InSAR can map surface displacements over wide areas with high spatial resolution on the order of 10 m or larger, by taking the differences between the phase values of SAR images at two acquisition epochs. InSAR has been used to detect secular and seasonal displacements over some thaw-related landforms in permafrost areas (e.g., Liu et al., 2010, 2014, 2015; Short et al., 2011; Iwahana et al., 2016; Molan et al., 2018; Antonova et al., 2018; Strozzi et al., 2018). In this study, we used L-band HH-polarized SAR images derived from the PALSAR-2 acquired by the Japanese Advanced Land Observing Satellite 2 (ALOS2) from 2015 to 2019 together with C-band VV-polarized SAR images taken during 2017-2018 derived from Sentinel-1 (Figure 2; see also Tables 1 and 2 for details). InSAR data processing was performed with the GAMMA software package (Wegmüller & Werner, 1997). To correct for topographic phases, we used TanDEM-X DEM (12m mesh). Compared to the former ALOS-1/PALSAR-1 InSAR, the ALOS2 orbit is well controlled, and the spatial baseline is much shorter, which allowed us to ignore DEM errors in the interferograms. The frequent data acquisition of Sentinel-1 since 2017 allowed us to examine the detailed seasonal changes in the surface deformation. The actual InSAR deformation map indicates the radar line-of-sight (LOS) changes that are derived by a projection of the surface 3D displacements onto the LOS direction, whereas the LOS is usually most sensitive to the vertical displacement as the incidence angles at the center of images are 36° and 39° for ALOS2 and Sentinel-1, respectively.

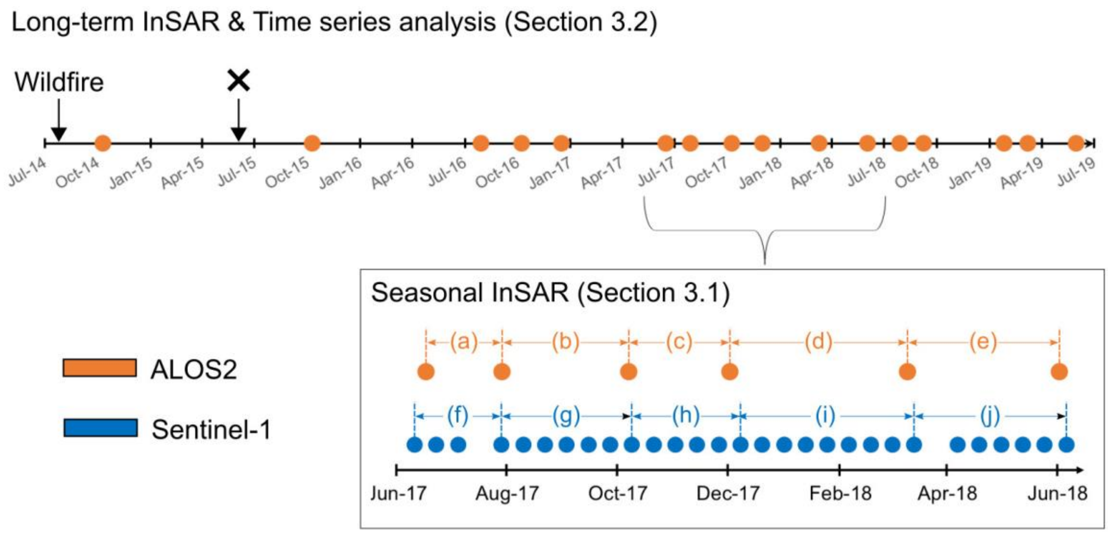

Figure 2. Schematic diagram of data time series. (Top) Long-term changes are derived from ALOS2 acquired on orange dots. Wildfire occurred from July to August 2014, and JAXA modified the center frequency of PALSAR-2 Beam No. F2-6 data in June 2015 shown with the cross. (Bottom) Short-term deformation during 2017-2018 as examined by Sentinel-1 images. We compare the ALOS2 and Sentinel-1 deformation maps during the five periods, (a)—(e) and (f)—(j).

Although L-band SAR is known to have better interferometric coherence than C-band SAR (e.g., Rosen et al., 1996), our results below indicated that the Sentinel-1 could maintain a comparable interferometric coherence with L-band ALOS2 even during winter season, probably owing to the short acquisition period of 12 days as well as the somewhat drier snow in the area. Some Sentinel-1 InSAR pairs in earlier summer, however, did not have good coherence. Moreover, ALOS2 has only imaged the area since 2014, but its data acquisition interval is much longer than that of Sentinel-1 (Figure 2). On the other hand, the frequent data acquisition in Sentinel-1 just started in 2017. In the following analysis, we used ALOS2 InSAR data to examine long-term deformation. As already noted in previous studies (Liu et al., 2014; Molan et al., 2018), it is not possible to infer the total subsidence using pre- and post-wildfire SAR images, as the dramatic changes in the land cover caused low interferometric coherence. Also, JAXA changed the carrier frequency of PALSAR-2 in June 2015. Thus, long-term deformation monitoring has been possible only since October 2015.

Meanwhile, we used Sentine-1 InSAR to examine short-term deformation and compared its data with ALOS2 interferograms, stacking Sentinel-1 interferograms to set the temporal coverages to be nearly identical with each other. During the temporal interval of ALOS2 images, Sentinel-1 repeated more cycles, so that the number of Sentinel-1 stack varied from three to eight. Because C-band InSAR phase is more sensitive to tropospheric delay errors, stacking allowed us to reduce the spatially random error phases. In contrast, L-band InSAR phase was more prone to ionospheric effect, which could be corrected for by range split-spectrum method (Gomba et al., 2016; Furuya et al., 2017). However, the spatial scale of ionospheric effects was much larger than that of the burned area, and the ionospheric signals were apparently non-correlated with the deformation signal. Thus, we simply took out the long-wavelength phase trend by fitting a low-order polynomial with clipped InSAR images after masking out the burned area. We also corrected for topography-correlated tropospheric errors when they clearly appeared in the InSAR image. These procedures were somewhat ad-hoc but allowed us to isolate relative displacements with respect to un-burned areas that were regarded as reference areas. It was also likely, however, that possible long-wavelength permafrost degradation signals, known as “isotropic thaw subsidence” (Shiklomanov et al., 2013), were eliminated. Yet, it would be challenging to detect isotropic thaw subsidence signal only from InSAR data. For the moment, we simply ignored such possible long-wavelength deformation signals.

In order to infer long-term temporal changes and cumulative displacements, we performed SBAS (Small Baseline Subset)-type time-series analysis (Berardino et al., 2002; Schmidt and Bürgmann, 2003), using ALOS2 interferograms. We could estimate the average LOS-change rates between each acquisition epoch without assuming any temporal change models. In contrast to the original SBAS approach, we did not estimate DEM errors because the well-controlled orbit as well as the precision TanDEM-X DEM have no sensitivities to those errors.

3 Results

3.1 Seasonal deformation and comparison of ALOS2/Sentinel-1 interferograms

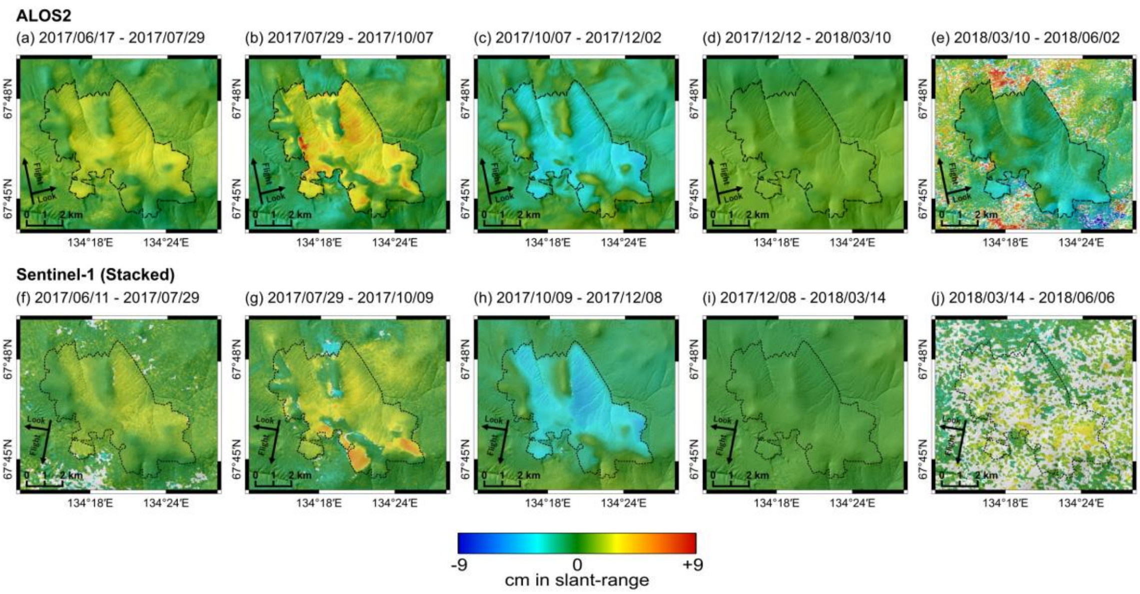

Figure 3. (Top) ALOS2 interferograms during the five periods, (a—e). (Bottom) Sentinel-1 stacked interferograms during the five periods, (f)—(j), derived so that the temporal coverage could nearly match those from (a) to (e); all the interferograms are overlaid on hill-shade maps. Warm and cold colors indicate LOS changes away from and toward the satellite, respectively. ALOS2 and Sentinel-1 imaging were performed by ascending and descending orbit, respectively, and both sensors were right-looking; details of each image are described in Tables 1 and 2.

In Figures 3, we compared the ALOS2 and stacked Sentinel-1 interferograms in the five periods, (a—e) (Figure 2); their differences are shown in Figures 4. Despite the differences in look directions, both ALOS2 and Sentinel-1 similarly indicate extensions in the LOS in the periods (a) and (b), and their deformation areas and amplitude were mostly consistent, suggesting that LOS changes were largely due to summer subsidence. In terms of the spatial distribution of deformation signals, we notice that the LOS changes over higher-elevation areas such as ridge and peak were insignificant, whereas the boundaries between the burned and un-burned areas were clear. During the period (c), both ALOS2 and Sentinel-1 indicated shortening in the LOS by an approximate 5 cm maximum, and the deformation areas and amplitude were quite similar. This observation presumably indicated frost heave in the early freezing period. In view of the previous two periods, both subsiding and uplifting areas were nearly the same. The following period (d) also included the winter season with much colder air temperatures, but we did not observe any significant deformation signals, indicating that frost-heave virtually stopped in early December.

While the good interferometric coherence during mid-winter was an unexpected result, we speculate that it could have been due to drier, lower amounts of snowfall, which would have allowed microwaves to reach the ground surface. In the periods (e) and (j), both ALOS2 and Sentinel-1 suffered from decorrelation, and we could not identify clear deformation signals. However, in light of Figures 5 below, each of the Sentinel-1 interferograms had overall good coherence with the exception of the data acquired in the middle of May. These observations suggested that the decorrelation may be attributable to the rapid changes on the ground surface during the initiation of thawing season, when the air temperature rises above the freezing point.

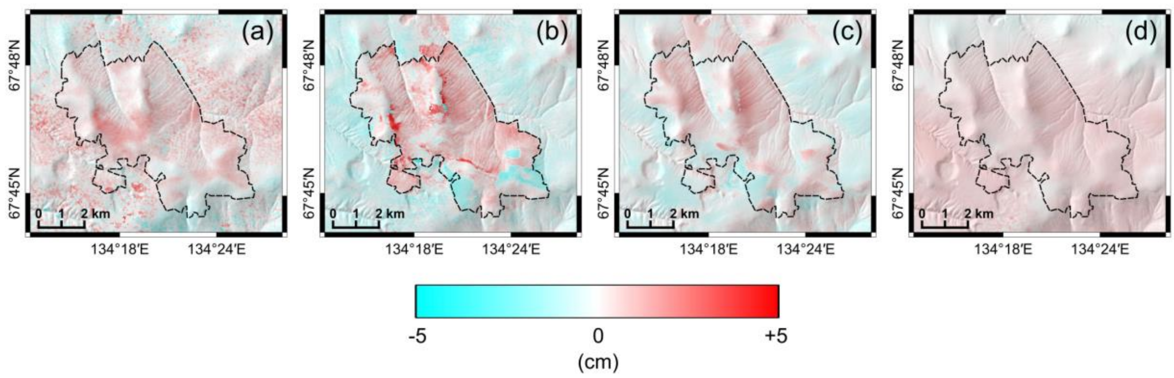

Figure 4. Differences in LOS-change detected by ALOS2 and Sentinel-1 seasonal interferograms (Figures 3a-d and 3f-i). In the last term of seasonal analysis (Figure 3e and 3j), we could not estimate differences due to coherence loss.

Figure 4 shows the differences between ALOS2 and Sentinel-1 InSAR data with nearly identical periods, which may help in evaluating the measurement errors and uncertainties. Although the view directions of ALOS2 and Sentinel-1 were different, the similar spatial distribution of deformation signals in Figures 3 allowed us to assume that the deformation signals were largely due to vertical displacement. The estimated differences and 2$\boldsymbol{\sigma}$ errors were 0.5±1.2cm (Fig 4a), 0.7±2.3cm (Fig 4b), 0.3±1.3cm (Fig 4c), and 0.6±0.3cm (Fig 4d), with an average of 0.5±1.5 cm.

The differences and errors were variable over time, probably because interferometric coherence depended on the season of image acquisitions. Specific maximum differences are found in Figure 4b. Those differences would be mainly attributable to the Sentinel-1 interferogram (Figure 3g) as unwrapping errors were found during the three interferograms, (4, 5, 9), shown later in Figures 5. However, those unwrapping errors were notably concentrated at specific locations near the ridge and the boundaries between the burned and unburned areas during the “deforming” seasons. We have confirmed the presence of low coherence bands along the unwrapping errors, which might suggest large phase jumps due to rapid displacements during the 12 days.

Original Sentinel-1 interferograms in 2017 are shown sequentially in Figures 5, which demonstrate that the progress of deformation was not at a constant rate. The most rapid deformation took place in June (periods 1 and 2) with no substantial deformation in July (period 3) and started to subside again in August (periods 4-6). We found that the subsidence occurred sporadically over time and space, and that the burned area did not uniformly subside. Moreover, Figure 5 demonstrates that the frost heave started in late September, which was missed in the periods (b) and (g) of Figure 3, and that the absence of any deformation signals lasted from early December to May of the following year. We will physically interpret the absence of deformation signals during the coldest season in a subsequent section.

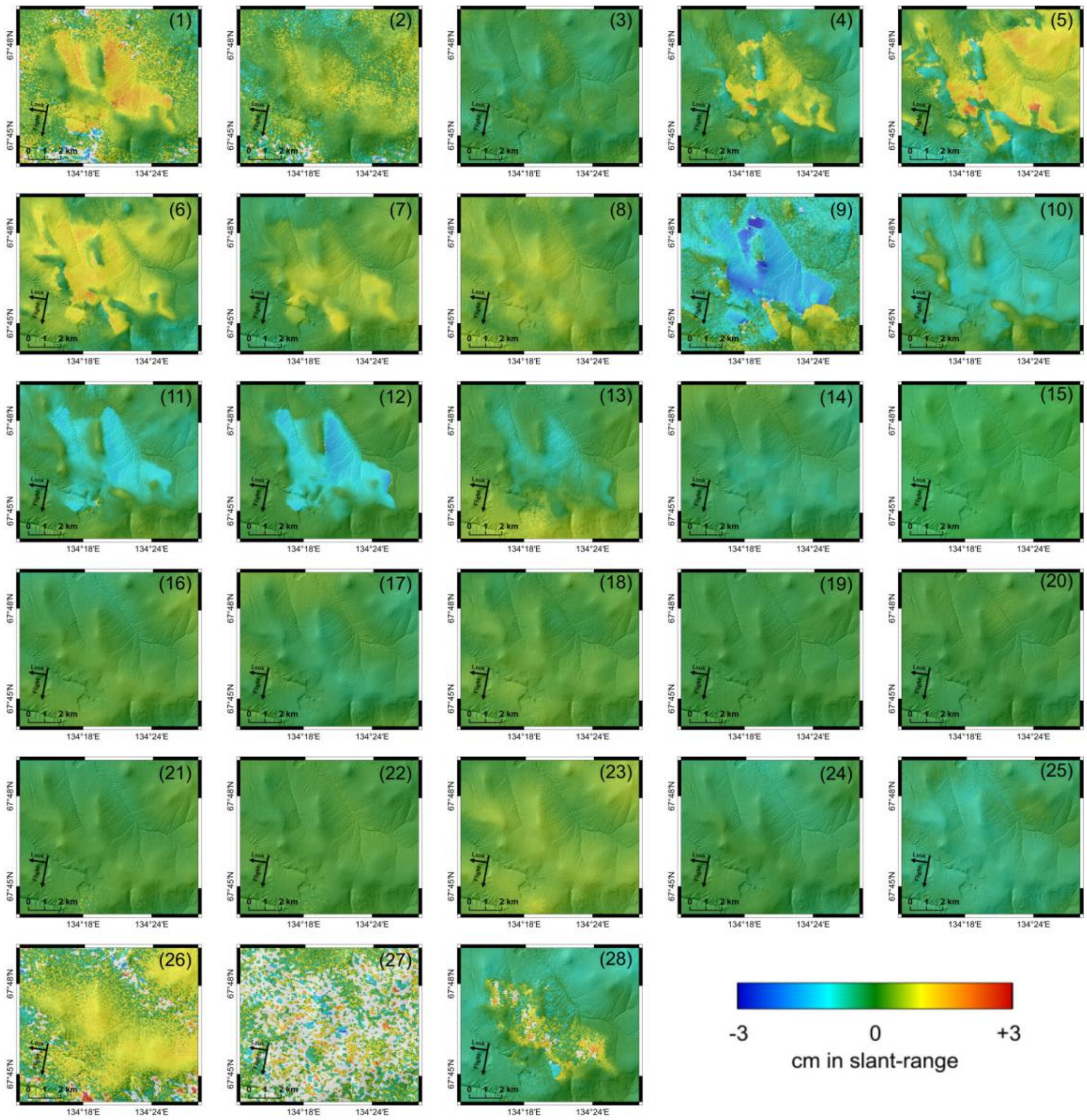

Figure 5. Sentinel-1 interferograms during the 27 periods from June 2017 through June 2018 overlaid on hill-shade map. Details of each image are described in Table 2.

3.2 Long-term deformation inferred from time-series analysis of ALOS2 interferograms

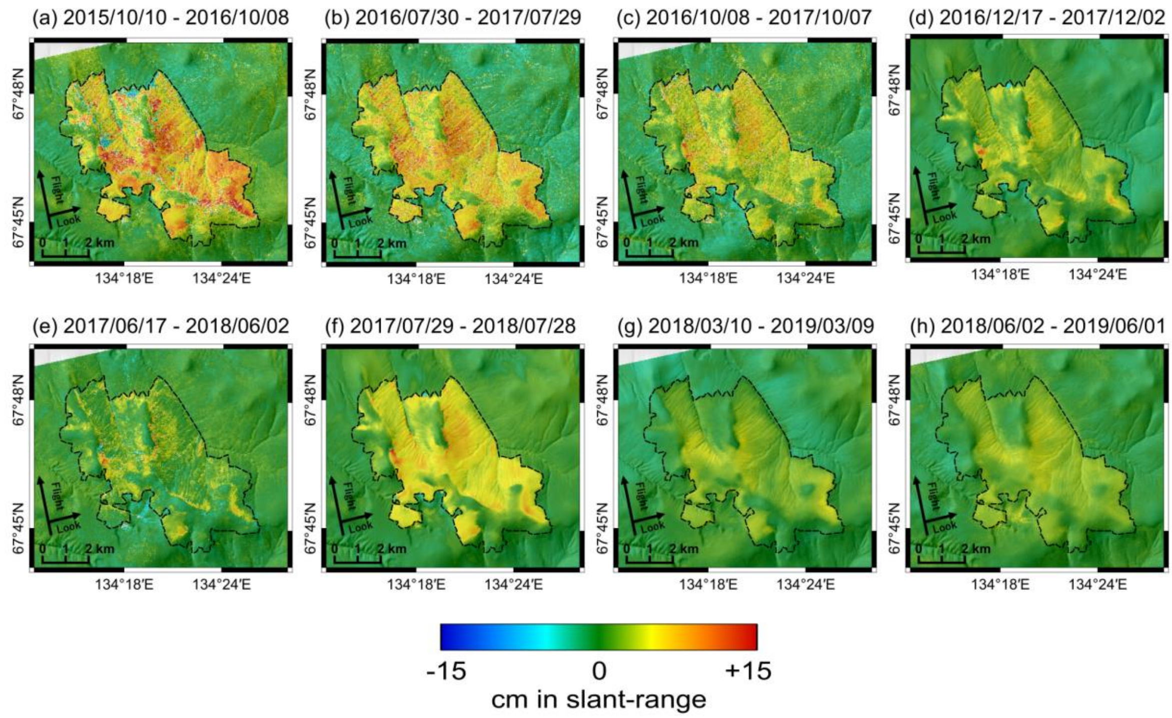

Figure 6. LOS-changes of ALOS2 interferograms overlaid on hill-shade map. Details of each image are described in Table 1; imaging was performed by ascending, right-looking orbit. Warm and cold colors indicate LOS changes away from and toward the satellite, respectively. Black dashed line indicates the boundary between the burned and unburned area confirmed with Landsat optical images.

Figures 6a—6h show ALOS2 interferograms, each of which covers nearly one-year after October 2015 with some overlaps in its temporal coverages. Figure 6a, derived at the earliest period after the fire, indicates the maximum one-year subsidence to be as much as 10 cm or more.

If the amplitude and timing of seasonal subsidence/uplift cycle are invariable over time, a one-year interferogram will tell us only the irreversible displacements regardless of the acquisition times of master/slave images, which corresponds to the “pure ice” model in Liu et al (2015). Figure 6 sequentially shows the periods from October 2015 to June 2019, and indicates that the yearly subsidence rate slowed down. However, the variations of the one-year LOS changes in Figures 6 suggest that the actual deformation processes were more complex.

In order to infer long-term temporal changes and cumulative displacements, we applied SBAS-type time series analysis, using 50 quality ALOS2 interferograms that included not only one-year interferograms but also short-term interferograms (Figures 7). Figure 8 shows the cumulative LOS changes from October 2015 to June 2019, and that the maximum LOS extension reached as much as 25 cm. Considering that the LOS changes during the first year after the 2014 fire were not included, the total LOS changes were presumably much greater than 25 cm, which meant that the subsidence was greater than 30 cm on account of the 36° incidence angle. As mentioned earlier, however, the higher-elevation areas such as the ridge did not undergo significant deformation, which probably would have been the case even during the first year after the fire.

We show the estimated time-series data at four representative sites (Figures 9a-9d), whose locations are indicated in the Figure 8. The sites (a) and (b) underwent nearly the same cumulative LOS changes by roughly 20 cm but were located at different slopes that are 4.3 km apart. On the other hand, the cumulative LOS changes at the site (d) were relatively small (approximately 10 cm). While there may have been actual differences in the deformation signals, it is possible that the west-facing slope may have contributed to the reduction of total LOS changes because of the present right-looking observation geometry, canceling the westward and downward displacements in the total LOS changes. The site (c) located in the ridge did not show either significant seasonal or long-term deformation.

Time series data in Figures 9a and 9b clearly indicate that the largest subsidence took place from 2015 and 2016. We believe, however, that the most significant subsidence probably occurred only during the thaw season in 2016, as we have observed, in previous section, that no deformation occurred from December to March. Thus, the actual subsidence rate in 2016 was likely to be much faster than that expected from the linear trend in Figures 9a and 9b.

In order to estimate the errors of the estimated time series, we assumed each original SAR scene contained 0.2 cm errors, and made InSAR data covariance matrix, following the method of Biggs et al. (2007). The errors are relatively smaller than those in previous studies of SBAS analysis (e.g. 0.4 cm in Schmidt et al., 2003; 0.75 cm in Biggs et al., 2007), because, as noted earlier, we took out the long-wavelength phase trend form each InSAR image, and the analysis area is smaller ($\mathbf{12 \times 12}$ km) than previous studies. The error bars in Figures 9a-9d indicate estimated standard deviation with $\mathbf{2\sigma}$, and reach ±1.5cm at the last period.

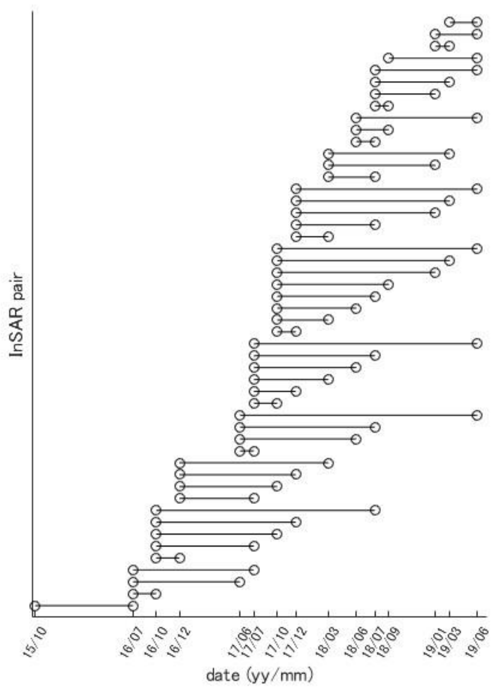

Figure 7. Temporal distribution of interferograms for the time-series analysis. 50 interferograms were generated from 15 ALOS2 SAR images.

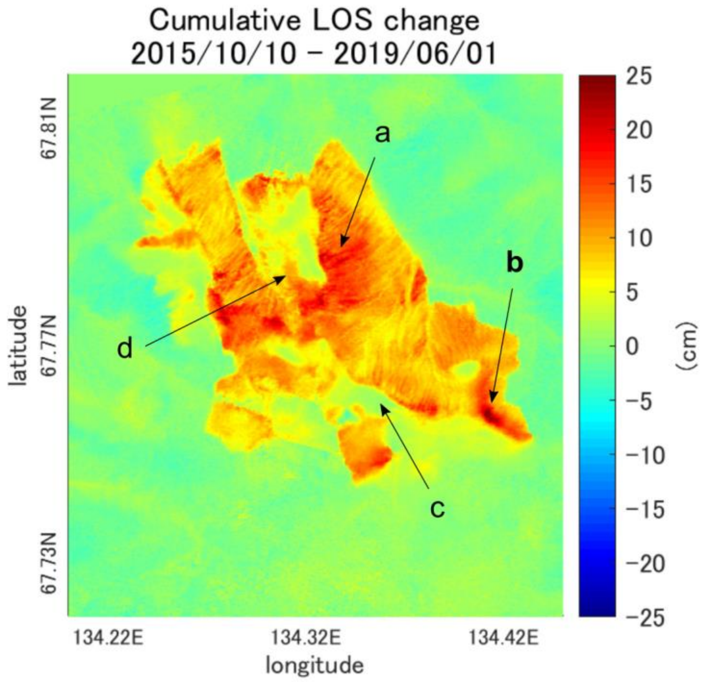

Figure 8. Cumulative LOS changes from 2015 to 2019 estimated by InSAR time-series analysis. The time series of LOS change at each site (a–d) is indicated in Figure 9.

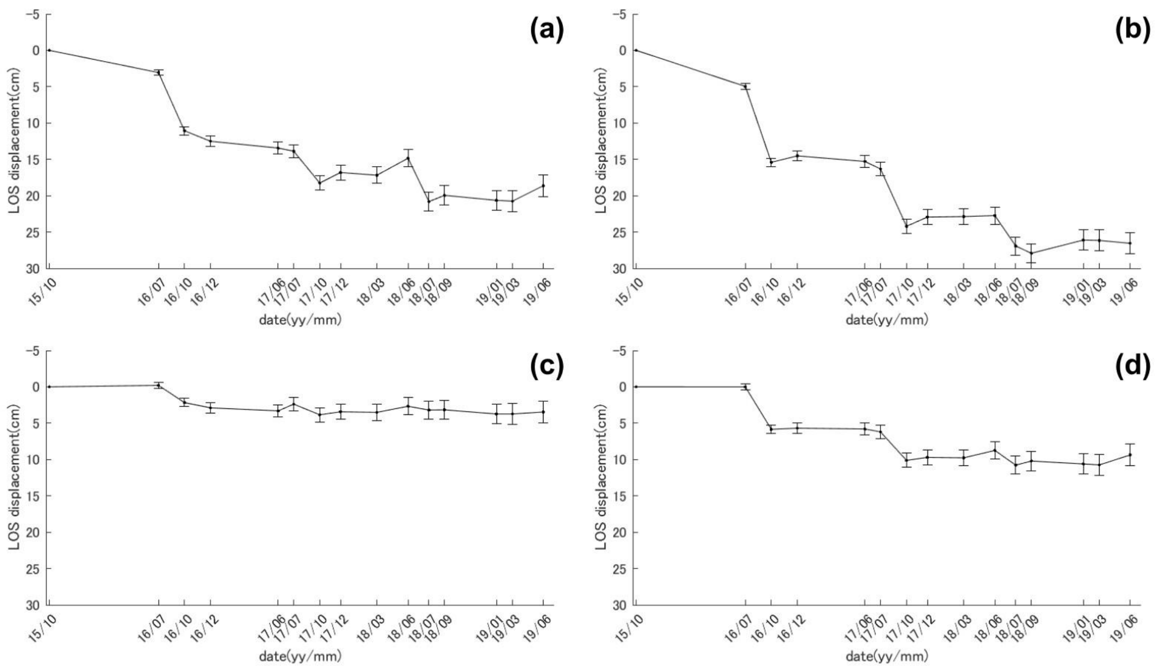

Figure 9. Panels (a–d) indicate the time series of LOS changes at each point indicated in Figure 8. Sites (a) and (b) are located at the east facing slope. Site (c) is located at the ridge, where no deformation signal was detected by original interferograms. Site (d) is at the west facing slope.

4 Discussion

4.1 Estimating the total volume of thawed excess ice

Post-wildfire deformation over a permafrost area presumably consists of two contributions: (1) irreversible subsidence due to melting of massive ice below the active layer, and (2) seasonally cyclic subsidence and uplift due to freeze-thaw of the active layer (Liu et al., 2014, 2015; Molan et al., 2018). In order to separate the two processes from the observed deformation data, Liu et al (2014) used independent ground-measured ALT data to predict the ALT contribution to total subsidence. Ground-measured pre-fire ALT data were not available at this study site. Given the temporal evolution of post-wildfire deformation data (Figures 9a-9d), however, we may regard the cumulative deformation in Figure 8 as being due to irreversible subsidence during the period between October 2015 and June 2019, and estimate the total thawed volume as $\mathbf{3.56 \pm 2.24 \times 10^6}$ m^3; the error bar is based on the root mean square of the no-deformation signals outside the burned area, which is multiplied by the burned area. However, in view of the temporal evolution in Figure 9, we could speculate that a much larger deformation was taking place immediately after the 2014 fire until October 2015, during which, unfortunately, no deformation data are available. Thus, this estimate should be viewed as a lower estimate, with the actual volume of thawed excess ice possibly being much greater.

Meanwhile, the volume of thawed excess ice depended on many factors such as burn severity, local vegetation, local ice content, and topography. Our results of the 2014 wildfire could become a reference for future works on the impact of the nearby 2019 wildfires around Batagay.

4.2 Interpretation of frost-heave signals based on premelting dynamics

We begin with a brief review of the microscopic physics of frost heave. Taking a soil particle inside a unit of ice, and owing to both the depression of freezing temperature due to the Gibbs-Thomson effect and the repulsive thermomolecular pressure between ice and soil particles (inter-molecular force), there exists an unfrozen (premelted) water film between the ice and soil particle, even below the bulk-melting temperature of 0 °C (e.g., Dash, 1989; Worster and Wettlaufer, 1999). In the presence of a temperature gradient, the repulsive thermomolecular pressure on the colder side is greater than that on the warmer side, and thus the net thermo-molecular force on the soil particle tends to move it toward the warmer side, a phenomenon known as thermal regelation (e.g., Worster and Wettlaufer, 1999; Rempel et al., 2004). Meanwhile, the premelted water migrates toward lower temperature, where ice lenses will be formed. These processes are responsible for frost heave and continue as long as the temperature gradient is maintained, or until significant overburden pressure is applied (e.g., Dash, 1989; Worster and Wettlaufer, 1999; Rempel et al., 2004).

Inspired by one-way frost heave experiments (Mutou et al., 1998; Watanabe and Mizoguchi, 2000), Worster and Wettlaufer (1999) and Rempel et al (2004) derived a steady-state heave rate $\boldsymbol{V_l}$ of an ice lens, taking into account the force balance among the thermo-molecular force $\boldsymbol{F_T}$, hydrodynamic force $\boldsymbol{F_\mu}$, and overburden force $\boldsymbol{F_O}$ (pressure $\boldsymbol{P_0}$). Below is a non-dimensional heave rate $\boldsymbol{v_l}$ of an ice lens as a function of its boundary position $\boldsymbol{\xi_l}$ given by Rempel et al (2004):

$$\boldsymbol{v_l \equiv \frac{\mu V_l}{k_0 \rho G} = \left[\int_0^{\xi_l} (1 - \phi S_s) d\xi - p_o\right] \left[\int_{\xi_h}^{\xi_l} \frac{(1 - \phi S_s)^2}{\widetilde{k}} d\xi\right]^{-1}},$$

where $\boldsymbol{\mu}$, $\boldsymbol{k_0}$, **and** $\boldsymbol{\rho}$ are the viscosity of water, the permeability of ice-free soil, density of water, respectively. The quantity $\boldsymbol{G} \equiv (\boldsymbol{L}/\boldsymbol{T_m})\langle \boldsymbol{\nabla T} \rangle$ has the same dimension as gravity and is responsible for thermo-molecular force when multiplied by the mass of displaced ice; $\boldsymbol{L}$ is the latent heat of fusion and $\boldsymbol{T_m}$ is the bulk melting temperature. The first and second term in the bracketed numerator are proportional to $\boldsymbol{F_T}$ and $\boldsymbol{F_O}$, respectively, while the bracketed denominator is proportional to $\boldsymbol{F_\mu}$. The integral is performed along $\boldsymbol{\xi} \equiv \boldsymbol{z}/\boldsymbol{z_f}$, where $\boldsymbol{z_f}$ is the position above (below) where ice saturation $\boldsymbol{S_s}$ becomes non-zero (zero); $\boldsymbol{z_h}$ indicates the position where hydrostatic pressure is achieved, and $\boldsymbol{\phi}$ is the porosity of soil. The normalized overburden pressure and permeability are defined as $\boldsymbol{p_0} \equiv \boldsymbol{P_0}/\boldsymbol{\rho G z_f}$ and $\widetilde{\boldsymbol{k}} \equiv \boldsymbol{k}/\boldsymbol{k_0} \geq \mathbf{1}$, respectively.

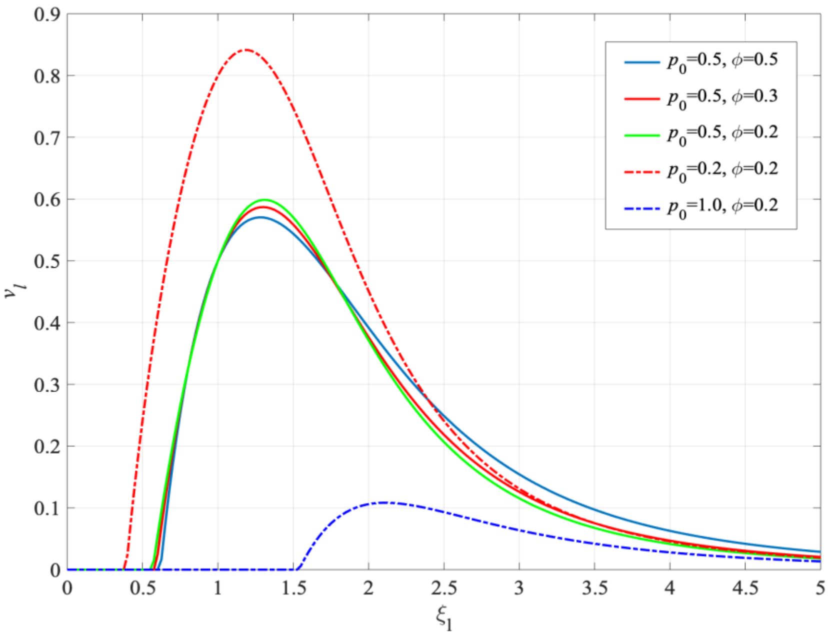

Figure 10. Non-dimensional heave rate profiles of an ice lens as a function of its boundary position, based on the analytical model by Rempel et al (2004). Five cases of non-dimensional overburden pressure $\boldsymbol{p_0}$ and porosity $\boldsymbol{\phi}$ are shown.

Figure 10 shows five cases of non-dimensional heave rate profiles as a function of the ice lens boundary position $\boldsymbol{\xi_l}$, indicating that the maximum heave rate is mainly controlled by the normalized overburden pressure $\boldsymbol{p_0}$ and is somewhat insensitive to the porosity $\boldsymbol{\phi}$. Details of the heave rate profiles will depend on the assumed models of permeability and ice saturation, but the qualitative characteristics are not altered (Rempel et al., 2004). There exist two positions that give the same heave rate, but only the branch with smaller $\boldsymbol{\xi_l}$ is stable (Worster and Wettlaufer, 1999; Rempel et al., 2004).

We can attribute the clear contrast in the frost heave signals inside and outside the burned area to the differences in the normalized overburden pressure $\boldsymbol{p_0}$. Because the mechanical overburden pressure $\boldsymbol{P_0}$ will not significantly differ from the inside to the outside of the burned area, the larger frost heave rate in the burned area would be caused by larger temperature gradient $\boldsymbol{G}$ and/or deeper frozen depth $\boldsymbol{z_f}$. Owing to the significant reduction in albedo over the burned area, the larger temperature gradient $\boldsymbol{G}$ than that of the unburned area is likely more marked in the early freezing season and may generate a greater thermomolecular force that will effectively reduce the overburden pressure. We may also interpret the absence of frost heave signals in mid-winter as due, probably, to the smaller temperature gradient $\boldsymbol{G}$ than that in late fall/early winter; if frost heave were controlled by temperature instead of temperature gradient, we would expect even more significant signals during the much colder part of the season. The deeper frozen depth $\boldsymbol{z_f}$ is also likely due to the loss of surface vegetation, and should supply more water for frost heave.

From the end of September to the middle of November 2017, Figure 5 shows LOS changes by approximately 1.5 cm over 12 days toward the satellite that corresponds to an approximate 1.9 cm uplift. Assuming a constant-rate frost heave, this corresponds to a heave rate of $\mathbf{1.8 \times 10^{-8}}$ (m/s). The most critical parameter controlling heave rate is the permeability for ice-free soil k_0, which can vary by orders-of-magnitude, while other parameters are well-constrained. We may fit our observed heave rate with the ice-free permeability, $\boldsymbol{k_0 \sim 10^{-17}}$ $(\mathbf{m^2})$, which is a likely value in view of the three cases in Rempel (2007).

5 Conclusions

We used L-band and C-band InSAR to detect post-wildfire ground deformation at Batagay in Sakha Republic, showing not only subsidence signal during the thawing season, but also uplift during the early freezing season and virtually no deformation in midwinter without loss of coherence. Time series analysis allowed us to estimate cumulative displacements and their temporal evolution, as quality interferograms could be obtained even in winter season. We found that the thawing of permafrost in the burned area lasted three years after the fire, but apparently slowed down after five years. Short-term interferograms (2017–2018) indicated that the subsidence and uplift was clearly enhanced compared with the unburned site. We have thus interpreted the frost heave signals within a framework of premelting dynamics. Post-wildfire areas are a focus of permafrost degradation in the Arctic region.

Acknowledgments, Samples, and Data

This study is supported by Researcher's Community Support Projects of Japan Arctic Research Network Center in 2016-2019, and by KAKENHI (19K03982). PALSAR2 level 1.1 data are provided by the PALSAR Interferometry Consortium to Study our Evolving Land Surface (PIXEL) and the ALOS2 RA6 project (3021) under cooperative research contracts with the JAXA. TanDEM-X DEM copyrighted by DLR and were provided under TSX proposal DEM_GLAC1864. Sentinel-1 SLC data are freely available. We downloaded the raw data from Copernicus Open Access Hub (https://scihub.copernicus.eu/). Both ALOS2 and TanDEM-X raw data are commercially available through the websites of PASCO CORPORATION (http://en.alos-pasco.com/) and WorldDEM Database (https://worlddem-database.terrasar.com/), respectively. We thank Go Iwahana for discussing our preliminary results.

References

Antonova, S., Sudhaus, H., Strozzi, T., Zwieback, S., Kääb, A., Heim, B., Langer, M., Bornemann, N., & Boike, J. (2018). Thaw Subsidence of a Yedoma Landscape in Northern Siberia, Measured In Situ and Estimated from TerraSAR-X Interferometry. *Remote Sens.*, 10(4):494, doi:10.3390/rs10040494.

Berardino, P., Fornaro, G., Lanari, R., & Sansosti, E. (2002). A New Algorithm for Surface Deformation Monitoring Based on Small Baseline Differential SAR Interferograms, *IEEE Trans. Geosci. Remote Sens.*, 40(11), 2375—2383. doi:10.1109/TGRS.2002.803792

Biggs, J., Wright, T., Lu, Z., & Parsons, B. (2007). Multi-interferogram method for measuring interseismic deformation: Denali Fault, Alaska. *Geophys. J. Int.*, 170(3), 1165–1179. doi:10.1111/j.1365-246X.2007.03415.x.

Chen, J., Günther, F., Grosse, G., Liu, L., & Lin, H. (2018). Sentinel-1 InSAR Measurements of Elevation Changes over Yedoma Uplands on Sobo-Sise Island, Lena Delta. *Remote Sens.*, 10, 1152; doi:10.3390/rs10071152.

Cherosov, M. M., Isaev, A.P., Mironova, S.I., Lytkina, L.P., Gavrilyeva, L.D., Sofronov, R.R., Arzhakova, A.P., Barashkova, N.V., Ivanov, I.A., Shurduk, I.F., Efimova, A.P., Karpov, N.S., Timofeyev, P.A., & Kuznetsova, L.V. (2010). Vegetation and human activity, in The Far North Plant Biodiversity and Ecology of Yakutia, edited by A. P. Isaev et al., 286 pp., Springer, New York.

Dash, J. G. (1989). Thermomolecular Pressure in Surface Melting: Motivation for Frost Heave, *Science*, 246, 1591-1593.

Dash, J. G., Rempel, A. W., & Wettlaufer, J. S. (2006). The physics of premelted ice and its geophysical consequences, *Rev. Mod. Phys.*, 78, 695—741. doi:10.1103/RevModPhys.78.695.

Furuya, M., Suzuki, T., Maeda, J., & Heki, K. (2017). Midlatitude sporadic-E episodes viewed by L-band split-spectrum InSAR, *Earth Planets Space*, 69:175. doi:10.1186/s40623-017-0764-6.

Gibson, C. M., Chasmer, L. E., Thompson, D. K., Quinton, W. L., Flannigan, M. D., & Olefeldt, D. (2018). Wildfire as a major driver of recent permafrost thaw in boreal peatlands, *Nature Comm.*, 9:3041, doi:10.1038/s41467-018-05457-1.

Gomba, G., Parizzi, A., Zan, F. D., Eineder, M., & Bamler, R. (2016). Toward operational compensation of ionospheric effects in SAR interferograms: The split-spectrum method, *IEEE Trans. Geosci. Remote Sens.*, 54 (3), 1446–1461. doi:10.1109/TGRS.2015.2481079

Günther, F., Grosse, G., Jones, B. M., Schirrmeister, L., Romanovsky, V. E., & Kunitsky, V. V. (2016). Unprecedented permafrost thaw dynamics on a decadal time scale: Batagay mega thaw slump development, Yana Uplands, Yakutia, Russia, AGU Fall Meeting San Francisco, USA, 12 December 2016 - 16 December 2016.

Hinkel, K. M. & Hurd, J. K. Jr. (2006). Permafrost Destabilization and Thermokarst Following Snow Fence Installation, Barrow, Alaska, U.S.A., AAAR, 38(4), 530-539.

Hu, F. S., Higuera, P. E., Walsh, J. E., Chapman, W. L., Duffy, P. A., Brubaker, L. B., & Chipman, M. L. (2010). Tundra burning in Alaska: linkages to climatic change and sea ice retreat. *J. Geophys. Res. Biogeosci*. 115, G04002, doi:10.1029/2009JG001270.

Iwahana, G., Uchida, M., Liu, L., Gong, W., Meyer, F. J., Guritz, R., Yamanokuchi, T., & Hinzman, L. (2016). InSAR Detection and Field Evidence for Thermokarst after a Tundra Wildfire, Using ALOS-PALSAR, *Remote Sens.*, 8, 218, doi:10.3390/rs8030218.

Jafarov, E. E., Romanovsky, V. E., Genet, H., McGuire, A. D., & Marchenko, S. S. (2013). The effects of fire on the thermal stability of permafrost in lowland and upland black spruce forests of interior Alaska in a changing climate, *Environ. Res. Lett*., 8, 035030, doi:10.1088/1748-9326/8/3/035030.

Jones, B. M., Grosse, G., Arp, C. D., Miller, E., Liu, L., Hayes, D. J., & Larsen, C. F. (2015). Recent Arctic tundra fire initiates widespread thermokarst development, *Sci. Rep*. 5, 15865; doi: 10.1038/srep15865.

Jorgenson, M. (2013). Thermokarst terrains, in Treatise on Geomorphology, vol. 8, edited by J. Shroder, R. Giardino, and J. Harbor, chap. Glacial and Periglacial Geomorphology, pp. 313–324, Academic Press, San Diego, Calif.

Kasischke, E., & Turetsky, M. (2006). Recent changes in the fire regime across the North American boreal region-spatial and temporal patterns of burning across Canada and Alaska, *Geophys. Res. Lett.*, 33, L09703, doi:10.1029/2006GL025677.

Kunitsky, V. V., Syromyatnikov, I. I., Schirrmeister, L., Skachk-ov, Y. B., Grosse, G., Wetterich, S. & Grigoriev, M.N. (2013). Ice-rich permafrost and thermal denudation in the Batagay area - Yana Upland, East Siberia, *Kriosfera Zemli* (Earth' Cryosphere), 17(1), 56-68. (in Russian)

Liu, L., Zhang, T., & Wahr, J. (2010). InSAR measurements of surface deformation over permafrost on the North Slope of Alaska. *J. Geophys. Res., Earth Surf.*, 115(3), 1–14, doi.org/10.1029/2009JF001547

Liu, L., Jafarov, E. E., Schaefer, K. M., Jones, B. M., Zebker, H. A., Williams, C. A., Rogan, J. & Zhang, T. (2014). InSAR detects increase in surface subsidence caused by an Arctic tundra fire, *Geophys. Res. Lett.*, 41, 3906–3913, doi:10.1002/2014GL060533.

Liu, L., Schaefer, K. M., Chen, A. C., Gusmeroli, A., Zebker, H. A., & Zhang, T. (2015). Remote sensing measurements of thermokarst subsidence using InSAR, *J. Geophys. Res., Earth Surf.*, 1935–1948, doi:10.1002/2015JF003599.

Mack, M., Bret-Harte, M., Hollingsworth, T., Jandt, R. R., Schuur, E. A. G., Shaver, G. R., & Verbyla, D. L. (2011). Carbon loss from an unprecedented Arctic tundra wildfire, *Nature*, 475, 489–492, doi:10.1038/nature10283.

Murton, J. B., Edwards, M. E., Lozhkin, A. V., Anderson, P. M., Savvinov, G. N., Bakulina, N., Bondarenko, O. V., Cherepanovah, M. V., Danilov, P. P., Boeskorov, V., Goslar, T., Grigoriev, S., Gubin, S. V., Korzun, J. A., Lupachev, A. V., Tikhonov, A., Tsygankova, V. I., Vasilieva, G. V., & Zanina, O. G. (2017). Preliminary paleoenvironmental analysis of permafrost deposits at Batagaika megaslump, Yana Uplands, northeast Siberia, *Quaternary Res.*, 87, 314–330, doi:10.1017/qua.2016.15.

Mutou, Y., Watanabe, K., Ishizaki, T. & Mizoguchi, M. (1998). Microscopic observation of ice lensing and frost heave in glass beads. In *Proc. Seventh Intl. Conf. on Permafrost*, June 23–27, 1998, Yellowknife, Canada (ed. A. G. Lewkowicz & M. Allard), pp. 283–287. Universite Laval, Montreal, Canada.

Molan, Y. E., Kim, J. W., Lu, Z., Wylie, B., & Zhu, Z. (2018). Modeling Wildfire-Induced Permafrost Deformation in an Alaskan Boreal Forest Using InSAR Observations, *Remote Sens.*, 10, 405; doi:10.3390/rs10030405.

Rempel, A. W., Wettlaufer, J. S. & Worster, M. G. (2004). Premelting dynamics in a continuum model of frost heave, *J. Fluid. Mech.*, 498, 227-224; doi: 10.1017/S0022112003006761

Rempel, A. W. (2007). Formation of ice lenses and frost heave, *J. Geophys. Res., Earth Surf*., 112, F02S21, doi:10.1029/2006JF000525.

Rosen, P. A., Hensley, S., Zebker, H. A., Webb, F. H., & Fielding, E. J. (1996). Surface deformation and coherence measurements of Kilauea Volcano, Hawaii, from SIR-C radar interferometry, *J. Geophys. Res., Planets*, 101(E10), 23,109—23,125, doi:10.1029/96JE01459.

Roshydromet (2008). Assessment report on climate change and its consequences in Russian Federation – General Summary. Moscow. http://climate2008.igce.ru/v2008/pdf/resume_ob_eng.pdf

Schirrmeister, L., Froese, D., Tumskoy, V., Grosse, G., & Wetterich, S. (2013). Yedoma: Late Pleistocene Ich-Rich Syngenetic Permafrost of Beringia, in *Encyclopedia of Quart. Sci*., 3, 542-552.

Schmidt, D. A. & Bürgmann, R. (2003). Time-dependent land uplift and subsidence in the Santa Clara valley, California, from a large interferometric synthetic aperture radar data set, *J. Geophys. Res.*, 108(B9), 2416, doi:10.1029/2002JB002267

Schuur, E. A. G., McGuire, A. D., Schädel, C., Grosse, G., Harden, J. W., Hayes, D. J., Hugelius, G., Koven, C. D., Kuhry, P., Lawrence, D. M., Natali, S. M., Olefeldt, D., Romanovsky, V. E., Schaefer, K., Turetsky, M. R., Treat, C. C. & Vonk, J. E. (2015). Climate change and the permafrost carbon feedback, *Nature*, 520, 171–179, doi:10.1038/nature14338.

Shiklomanov, N. I., Streletskiy, D. A., Little, J. D., & Nelson, F. E. (2013). Isotropic thaw subsidence in undisturbed permafrost landscapes, *Geophys. Res. Lett.*, 40, 6356–6361, doi:10.1002/2013GL058295.

Short, N., Brisco, B., Couture, N., Pollard, W., Murnaghan, K., Budkewitsch, P. (2011). A comparison of TerraSAR-X, RADARSAT-2 and ALOS-PALSAR interferometry for monitoring permafrost environments, case study from Herschel Island, Canada, *Remote Sens. Environ.*, 115, 3491—3506, doi:10.1016/j.rse.2011.08.012

Siberian Times (2019). https://siberiantimes.com/other/others/news/hell-on-fire-raging-bush-inferno-at-batagai-depression-giant-gash-in-the-tundra/

Strozzi, T., Antonova, S., Günter, F., Mätzler, E., Vieira, G., Wegmüller, U., Westermann, S. & Bartsch, A. (2018). Sentinel-1 SAR Interferometry for Surface Deformation Monitoring in Low-Land Permafrost Areas, *Remote Sens.*, 10, 1360, doi:10.3390/rs10091360

Taber, S. (1929). Frost heaving, *J. Geol*., 37:428–461. doi:10.1086/623637

Taber, S. (1930). The mechanics of frost heaving, *J. Geol*., 38:303–317. doi:10.1086/623720

Wagner, A. M., Lindsey, N. J., Dou, S., Gelvin, A., Saari, S., Williams, C., Ekblaw, I., Ulrich, C., Borglin, S., Morales, A., Ajo-Franklin, J. (2018). Permafrost Degradation and Subsidence Observations during a Controlled Warming Experiment, *Sci. Rep*., 8:10980, doi:10.1038/s41598-018-29292-y

Watanabe, K. & Mizoguchi, M. (2000). Ice configuration near a growing ice lens in a freezing porous medium consisting of micro glass particles, *J. Cryst. Growth*, 213, 135–140.

Wegmüller, U., & Werner, C. L. (1997). Gamma SAR processor and interferometry software. Proc. of the 3rd ERS Symposium, European Space Agency Special Publication, (ESA SP-414), 1687–1692.

Wettlaufer, J. S. & Worster, M.G (2006). Premelting Dynamics, *Annu. Rev. Fluid Mech.*, 38:427–52

Worster, M. G., & Wettlaufer, J. S. (1999). The fluid mechanics of premelted liquid films. In Fluid Dynamics at Interfaces (ed. W. Shyy & R. Narayanan), pp. 339–351. Cambridge University Press.

Yoshikawa, K., Bolton, W. R., Romanovsky, V. E., Fukuda, M., & Hinzman, L. D. (2002). Impacts of wildfire on the permafrost in the boreal forests of Interior Alaska, *J. Geophys. Res.*, 107(D1), 8148, doi:10.1029/2001JD000438.

Zhang, Y., Wolfe, S. A., Morse, P. D., & Fraser, I. O. R. H. (2015). Spatiotemporal impacts of wildfire and climate warming on permafrost across a subarctic region, Canada, *J. Geophys. Res. Earth Surf.*, 120,2338–2356, doi:10.1002/2015JF003679.

Table 1. Data list of ALOS2 for interferograms in Figures 3a-3e and Figure 6.

Interferogram	Dates (YYYYMMDD)	Perpendicular Baseline (m)	Temporal Baseline (days)
Short-term images (Figure 3)			
(a)	20170617-20170729	11	48
(b)	20170729-20171009	-104	72
(c)	20171009-20171202	-46	54
(d)	20171202-20180310	283	98
(e)	20180310-20180602	-259	84
Long-term images (Figure 6)			
(a)	20151010-20161008	98	364
(b)	20160730-20170729	97	364
(c)	20161008-20171007	-104	364
(d)	20161217-20171202	-146	350
(e)	20170617-20180602	-118	350
(f)	20170729-20180728	-200	364
(g)	20180310-20190309	-191	364
(h)	20180602-20190601	41	364

Table 2. Data list of Sentinel-1 for Stacked images in Figures 3f-3j and interferograms in Figure 5.

Stack	Interferogram	Dates (YYYYMMDD)	Perpendicular Baseline (m)	Temporal Baseline (day)
(f)	(1)	20170611-20170623	23	12
	(2)	20170623-20170705	-74	12
	(3)	20170705-20170729	-15	24
(g)	(4)	20170729-20170810	43	12
	(5)	20170810-20170822	-30	12
	(6)	20170822-20170903	36	12
	(7)	20170903-20170915	-15	12
	(8)	20170915-20170927	-54	12
	(9)	20170927-20171009	35	12
(h)	(10)	20171009-20171021	80	12
	(11)	20171021-20171102	32	12
	(12)	20171102-20171114	-46	12
	(13)	20171114-20171126	-89	12
	(14)	20171126-20171208	26	12
(i)	(15)	20171208-20171220	114	12
	(16)	20171220-20180101	43	12
	(17)	20180101-20180113	-66	12
	(18)	20180113-20180125	-143	12
	(19)	20180125-20180206	34	12
	(20)	20180206-20180218	59	12
	(21)	20180218-20180302	26	12
	(22)	20180302-20180314	-25	12
(j)	(23)	20180314-20180407	-91	24
	(24)	20180407-20180419	-43	12
	(25)	20180419-20180501	155	12
	(26)	20180501-20180513	-29	12
	(27)	20180513-20180525	-74	12
	(28)	20180525-20180606	-73	12